

Analysis and Optimization of Mixing Performance of the High-Temperature Gas Flow in a Mixing Chamber

J. Chu, D. Zhu, W. Wang, B. Li, J. Du and G. Yang[†]

*School of Mechanical Science & Engineering, Huazhong University of Science and Technology, WuHan
 HuBei 430074, China*

[†]Corresponding Author Email: yg_xing73@hust.edu.cn

(Received August 9, 2022; accepted November 16, 2022)

ABSTRACT

A high-temperature gas mixing chamber is a type of mechanical device which has been widely used to obtain airflow at a specific high temperature. When a temperature environment test for aviation equipment is performed, the airflow temperature should exceed 1,000 K and change fast. However, the existing mixing devices cannot meet the requirements for mixing speed and uniformity of temperature environment tests. To solve the problem of low mixing speed and uniformity, this paper proposes an innovative gas mixing chamber design. The proposed design allows cold and hot gases to be injected in directions perpendicular to each other, which increases the collision and heat exchange of gases with different temperatures. In this way, a faster mixing process and a more uniform outlet temperature field are obtained. Moreover, a genetic optimization method is used to improve the performance of a mixing chamber. This method considers temperature distribution, the velocity distribution of the outlet airflow, and the mixing speed. Simulation results show that the proposed method can reduce the mixing time from 4.4 s to 2.3 s, the standard deviation of the outlet temperature distribution from 25.2 to 14.7, and the standard deviation of velocity distribution from 1.3 to 0.36. The experimental results show good consistency with the simulation results, indicating that the simulation and optimization results are reliable, and the mixing performance of the cold and hot gas mixing chamber is significantly improved by the proposed method. The proposed method is important for optimizing the design of similar orifice plates and flow mixing structures.

Keywords Mixing chamber; Temperature field; Heat exchange; Structure optimization; Mixing performance.

NOMENCLATURE

σ_T	standard deviation of temperature at the outlet	ρ	fluid density;
Δt	mixing time	m	number of samples for correlation value calculation
σ_v	standard deviation of velocity at the outlet	t	time;
n	number of testing points at the outlet	\mathbf{u}	fluid velocity;
T_i	temperature of the i th testing point	u , v , and w	x , y , and z components of the fluid velocity vector;
\bar{T}	average temperature of the testing point at the outlet	S_u , S_v , and S_w	source terms of the momentum equation;
v_i	velocity of the i th testing point	T	temperature;
\bar{V}	average velocity of the testing point at the outlet	λ	thermal conductivity;
ρ	Spearman correlation value	c	specific heat capacity;
d_i	equivalence difference between two series of data for correlation value calculation	S_T	heat source volume.

1. Introduction

A high-temperature gas mixing chamber represents a gas-gas direct heat exchanger for gas mixing at different temperatures. A gas-gas heat exchanger has been widely used in the industry (Yee *et al.* 1990; Yan *et al.* 1999). Compared with other heat exchanger devices, a gas-gas heat exchanger has the advantages of simple structure, high heat transfer efficiency, and low manufacturing costs (Karana *et al.* 2021). Due to these advantages, a gas-gas heat exchanger has been widely used in industrial applications that require temperature control, such as the aviation industry (Asif *et al.* 2021).

When aircraft fly at a hypersonic speed, the air is strongly compressed and subjected to intense friction, and most of the kinetic energy is converted into thermal energy. In addition, a large amount of aerodynamic heat is generated at the apex of the aircraft head or at the leading edge of the wing, and the instantaneous temperature may rise to 1,600 K (Zhao *et al.* 2018; Zou *et al.* 2018). Therefore, for security reasons, it is necessary to add a gas temperature signal to the temperature environment test for aircraft (Zhao *et al.* 2020).

The surface temperature of aircraft changes rapidly, which requires using a fast-changing temperature signal in the tests. Generating a high-temperature gas signal in a temperature environment test for aircraft has become an urgent challenge. A heat exchanger has been widely applied to temperature environment tests. Recently, numerous studies on mixing devices have been conducted, and different designs have been proposed to improve the mixing performance (Badenhorst 2020). Vázquez *et al.* (2016) studied the recovery of methanol-water vapor heat waste using water as a heat transfer medium. Tang *et al.* (2019a) conducted a comparative analysis of the aligned elliptical tube and honeycomb circular tube in flue gas heat exchangers. Considering the temperature control in the flight environment simulation, Zhu (2021) obtained the airflow from 250 K to 265 K at the outlet of the heat exchanger by mixing the hot air at 373 K with the cold air at 233 K. However, in the aforementioned studies, usually thin plates or pipes have been designed inside a mixing device to improve the mixing performance, but the distribution and size of spoiler structures can produce different flow characteristics.

Indirect heat exchange through other media is not nearly as fast as direct mixing. However, using a direct mixing heat exchanger may cause the uniformity problem of airflow distribution at the outlet. Thus, a gas mixing device with a fast mixing speed and uniform outlet airflow is needed.

For improving the performance of a gas mixing chamber, the structural design is particularly important, and applying advanced optimization methods can help. Much research effort has been devoted to the optimization of mixing structural

design in recent years. Optimization of the inlet parameters of the mixing devices can improve their performance (Filip and Melichar 2021). Badenhorst (2020) optimized a plate heat exchanger for latent thermal energy storage using graphite composites. The author used simulated annealing and branch and bound algorithms to solve the optimization problem. Xie *et al.* (2020) used the genetic algorithm (GA) for the optimal design of a plate-fin heat exchanger (PFHE). Mishra (2004) performed the second law-based optimization of cross-flow plate-fin heat exchangers using the GA, considering the minimization of entropy generation units as an objective function. Mishra and Das (2009) used the GA for the optimal design of plate-fin heat exchangers, and good results were achieved using relevant optimization methods. The GA has achieved success in the structural optimization of mixing devices. Since a gas mixing chamber has multiple optimization objectives, this paper adopts an improved GA to design the mixing chamber.

Considering the demand for a temperature environment test for aviation equipment, this paper aims to design a gas mixing chamber that can rapidly generate high-temperature gas signals. To improve the mixing speed and the uniformity of the outlet airflow, an optimization strategy combining GA is applied. First, the initial gas mixing chamber is presented, and its mixing characteristics are studied using the CFD method. Next, the mixing performances for different structural designs are compared using the control variate method. Then, structure size optimization is performed to establish an optimal mixing performance structure. Finally, the performances of the proposed structure before and after the optimization are compared.

This paper is organized as follows: Section 1 introduces the background and significance of the research. Section 2 analyzes the working principle and initial design of a mixing chamber. Section 3 explores the effects of structural parameters. Section 4 explains the optimization of a gas mixing chamber by the NSGA-II, and Section 5 describes the experiment and analysis. Section 6 concludes the paper.

2. INITIAL DESIGN ANALYSIS

2.1 Working Principle of a Mixing Chamber

Compared to the ordinary non-contact heat exchanger, a direct heat exchanger has higher heat exchange efficiency (Riley *et al.* 2019). In this paper, the hot and cold gases are directly mixed by feeding them into a mixing chamber to obtain a high-temperature gas signal at the outlet. The structure of the gas mixing chamber is shown in Fig. 1, where it can be seen that it consists of the plasma torch, ceramic inner chamber, insulation foam, and protective shell. The hot gas is heated rapidly by the plasma torch and then mixed with the cold gas in the ceramic inner chamber. To reduce the heat exchange

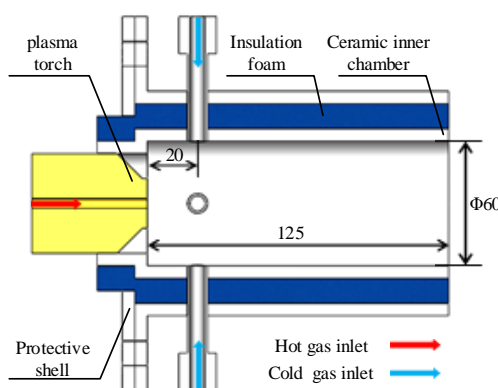


Fig. 1. Initial model of the mixing chamber.

plasma torch and then mixed with the cold gas in the ceramic inner chamber. To reduce the heat exchange with the outside environment during the mixing process, insulation foam is used between the ceramic inner chamber and the protective shell. For the uniformity of the gas outlet, one hot gas inlet and four evenly distributed cold gas inlets are designed. Moreover, the mixing speed increases when a multi-cold gas inlet is used.

Considering the gas stability at high temperatures, an inert gas, nitrogen, is used as a mixing gas. Mizeraczyk et al. (2000) obtained high-temperature plasma by heating nitrogen gas with a plasma torch. A gas flow ranging from 2,000 K to 10,000 K was obtained by adjusting the heating power and the flow rate of the nitrogen. In this paper, nitrogen gas heated by a plasma torch is used as hot gas in a gas mixing chamber, and nitrogen at room temperature is used as cold gas in the gas mixing chamber.

2.2 CFD Simulation and Evaluation Method

The mixing uniformity and the mixing speed are key performance metrics of the mixing chamber. However, since the mixing process of hot and cold gases is a complex thermodynamic process, it is difficult to obtain the mixing results by theoretical derivation. Currently, computational fluid dynamics (CFD) represents an important method for studying fluid mixing problems. Numerical calculations based on the CFD can accurately simulate the flow characteristics for different structural parameters. The CFD model is given by Eq. (1), which satisfies the energy conservation law, the mass conservation law, and the momentum conservation law.

$$\left\{ \begin{array}{l} \frac{\partial \rho}{\partial t} + \nabla \cdot (\rho \mathbf{u}) = 0 \\ \frac{\partial (\rho u)}{\partial t} + \nabla \cdot (\rho \mathbf{u} \mathbf{u}) = \nabla \cdot (\mu \nabla \mathbf{u}) + S_u \\ \frac{\partial (\rho v)}{\partial t} + \nabla \cdot (\rho \mathbf{u} \mathbf{v}) = \nabla \cdot (\mu \nabla \mathbf{v}) + S_v \\ \frac{\partial (\rho w)}{\partial t} + \nabla \cdot (\rho \mathbf{u} \mathbf{w}) = \nabla \cdot (\mu \nabla \mathbf{w}) + S_w \\ \frac{\partial (\rho T)}{\partial t} + \nabla \cdot (\rho \mathbf{u} T) = \nabla \cdot \left(\frac{\lambda}{c} \nabla T \right) + S_T \end{array} \right. \quad (1)$$

In Eq. (1),

ρ : fluid density;

t : time;

\mathbf{u} : fluid velocity;

u , v , and w : x , y , and z components of the fluid velocity vector;

S_u , S_v , and S_w : source terms of the momentum equation;

T : temperature;

λ : thermal conductivity;

c : specific heat capacity;

S_T : heat source volume.

The numerical calculation model of the mixing chamber was established using the CFD method. The analysis was performed using the flow field simulation software FLUENT. Considering fluid turbulence, the turbulence model was selected as an RNG $K-\epsilon$ model, which could ensure better precision than the standard $K-\epsilon$ model. The operating fluid was nitrogen. The boundary condition of the hot gas inlet was defined by a temperature of 1,500 K and a flow rate of 10 L/min.

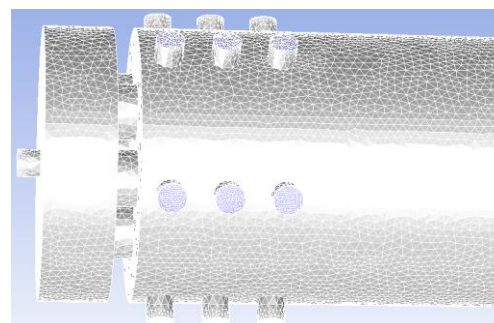


Fig. 2. Simulation model with total element number of 262696.

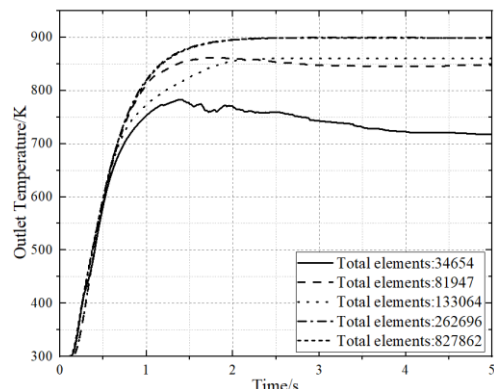


Fig. 3. Outlet temperature curve with different total element numbers.

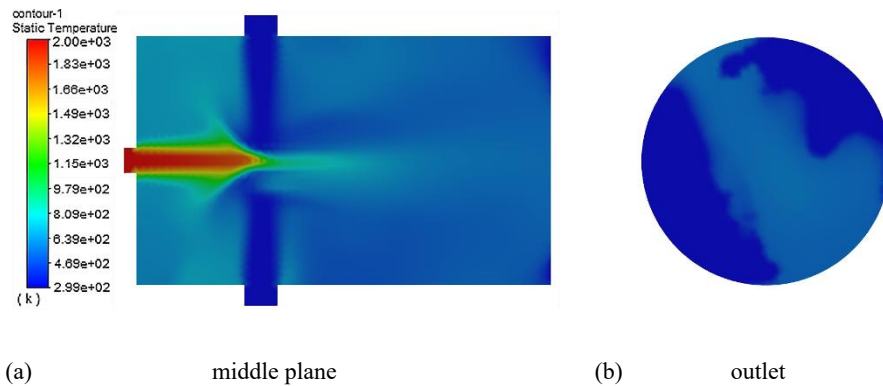


Fig. 4. Temperature contour of the gas mixing chamber.

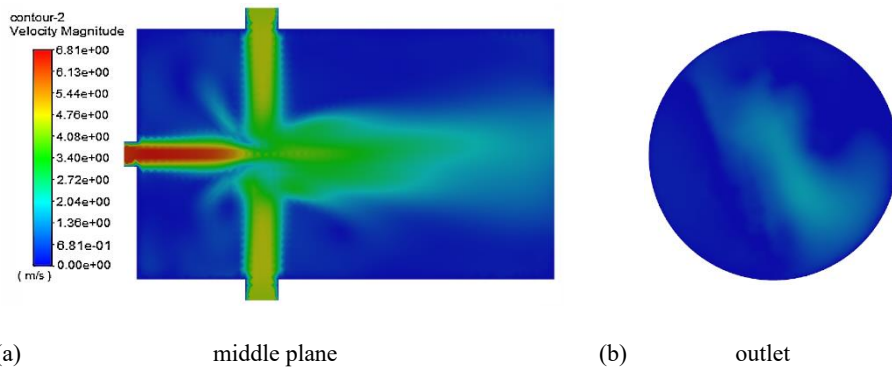


Fig. 5. Velocity contour of the gas mixing chamber.

The boundary condition of the cold gas inlet was defined by a temperature of 300 K and a flow rate of 40 L/min. The inner chamber diameter and length were 60 mm and 125 mm, respectively. The distance between the cold gas inlets and the hot gas inlet was 20 mm.

Before performing simulations, grid independence was verified. The simulation model with a total element number of 262696 is shown in Fig. 2. In addition, simulations were carried out for different total element numbers, namely 34654, 81947, 133064, 262696, and 827862. The simulation results are shown in Fig. 3. There were significant differences in the outlet temperature when the total element number was less than 262696. However, the outlet temperature remained consistent when the total element number was more than 262696. Hence, it is best to choose a total element number near 260000.

The temperature and velocity contours at the middle plane and outlet section of the gas mixing chamber are shown in Figs. 3 and 4, respectively.

As shown in Figs. 4 and 5, the temperature and velocity at the outlet were not uniformly distributed, which indicated that the hot and cold gases mixed incompletely. However, the mixing uniformity and speed cannot be accurately described by pictures. Therefore, a quantitative description of the mixing

uniformity and mixing speed is given in the following.

The relationship between the outlet temperature and the flow time was obtained by the Fluent simulations, as shown in Fig. 6. It was considered that the steady state was reached when the outlet temperature changed no more than ± 10 K. The mixing time Δt denoted the time needed for the outlet temperature to reach a steady state; a shorter mixing time Δt indicated a faster mixing speed.

A mixing chamber with good mixing performance should have even temperature and velocity distributions. In this study, standard deviation σ_T

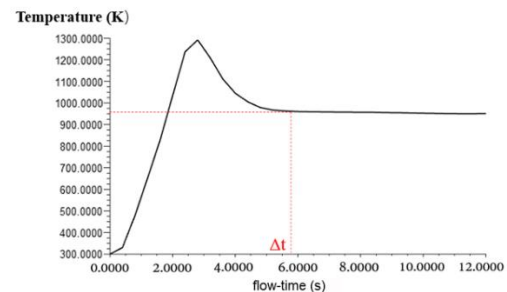


Fig. 6. Relationship between the outlet temperature and the mixing time.

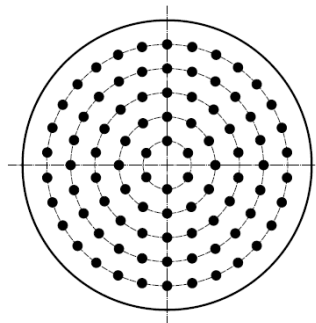


Fig. 7. Sampling points at the outlet.

of the temperature distribution and the standard deviation σ_T of the velocity distribution were used to describe the mixing uniformity. To obtain the mixing data at the outlet section, five circles were extracted uniformly, and multiple points were selected uniformly on each radius. The number of sampling points on each circle was proportional to the radius. Finally, a total of 90 points were selected in the outlet section to obtain dispersive temperature and velocity values, as shown in Fig. 7.

After exporting data of each point by the Fluent, σ_T and σ_v were calculated as follows:

$$\sigma_T = \sqrt{\frac{1}{n} \sum_{i=1}^n (T_i - \bar{T})^2} / \bar{T} \quad (2)$$

$$\sigma_v = \sqrt{\frac{1}{n} \sum_{i=1}^n (V_i - \bar{V})^2} / \bar{V} \quad (3)$$

where T_i and V_i denote the temperature and velocity value of the i th point.

2.3 Initial Chamber Design

For a given working condition, the mixing speed and the airflow distribution at the outlet were directly affected by the diameter and length of the chamber. The mixing performance of the mixing chamber with a different size was compared and analyzed by the CFD method. First, the diameter was kept fixed at 60 mm, and the length of the chamber was changed, having values of 50 mm, 75 mm, 100 mm, 125 mm, and 150 mm. The mixing performance results are shown in Table 1. The mixing time Δt and gas distribution at the outlet were both affected by the chamber length. The longer the chamber length was, the smaller the σ_T and σ_v values were, which meant that the velocity and temperature distributions of the gas at the outlet were more uniform when the chamber length was longer. However, under a longer chamber length, more time was needed to reach a steady state. Moreover, while the length exceeded 100 mm, there was a significant increase in the mixing time, but σ_T and σ_v values did not drop much. Therefore, the initial chamber length was designed to be 100 mm.

At the chamber length of 100 mm, the chamber diameter was set to 30 mm, 40 mm, 50 mm, 60 mm,

and 70 mm. The mixing performance results are shown in Table 2. The increase in the chamber diameter reduced the mixing time when the diameter was less than 50 mm but increased the mixing time when the diameter was longer than 50 mm. The changing trend of the gas distribution at the outlet was similar. Hence, the initial value of the chamber diameter was designed to be 60 mm.

The main parameters of the initial design of the mixing chamber are shown in Table 3.

Table 1 Mixing performance at different chamber lengths.

Length (mm)	σ_T	σ_v	Δt (s)
50	40.6	2.7	2.1
75	35.1	2.3	3.4
100	26.1	1.4	5.8
125	24.2	1.4	8.6
150	20.4	1.2	11.1

Table 2 Mixing performance of different diameters.

diameter (mm)	σ_T	σ_v	Δt (s)
30	29.6	1.9	8.2
40	27.1	2.1	7.3
50	28.3	1.7	5.5
60	26.1	1.4	5.8
70	30.2	1.6	7.4

Table 3 Main parameters of the gas mixing chamber.

Parameter (unit)	Value
Operating fluid	nitrogen
Hot gas flow rate (L/min)	10
Cold gas flow rate (L/min)	40
Hot gas temperature (K)	1500
Cold gas temperature (K)	300
Inner chamber diameter (mm)	60
Inner chamber length (mm)	100
Diameter of inlets (mm)	6
Number of cold gas inlets	4

3. Effects of Structural Parameters

According to the simulation results, the cold and hot gases collided with each other and exchanged heat while flowing together to the outlet. However, the temperature and velocity distributions at the outlet section showed a decreasing trend from the center outward. Thus, the mixing speed should be improved further. To improve the structure capability, different mixing chamber structures were analyzed to study the effect of the mixing chamber's structural parameters on its mixing performance. The effect of a mixing device

structure has been analyzed in previous studies by the CFD method. [Habibi et al. \(2019\)](#) analyzed the effect of the number of fuel nozzles on the

combustion effect in combustion chamber optimization. [Wang et al. \(2017\)](#) compared the effects of different injection angles on the mixing process of the hollow-cone spray in a confined high-temperature gas cross-flow. It was concluded that the injection angle directly affected the interaction between the two fluids. [Tang et al. \(2019b\)](#) optimized a throttle orifice plate using the GA to improve pressure distribution in the flow field. The aforementioned studies have been the main motivation to investigate the structure of different cold and hot gas inlets and the orifice plate. Because the size of the heating device is fixed, the parameters of the hot gas inlet remained unchanged. The numbers and injection angles of cold gas inlets were reconsidered, and the mixing performance of different structures was compared using the control variate method.

Due to the uniformity of the outlet airflow, the gas inlet was circumferentially homogeneously distributed. Structures with different numbers of cold gas inlets per circle are shown in Fig. 8.

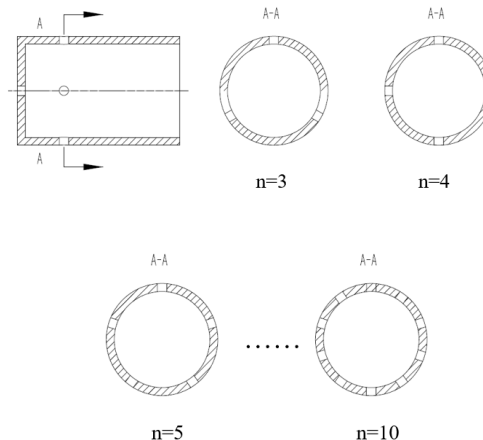


Fig. 8. Structures with different numbers of cold gas inlets per circle.

3.1 Number of Cold Gas Inlets Per Circle

When the other conditions were the same as those in Table 3, the mixing performance results for different numbers of cold gas inlets per circle were calculated, as shown in Table 4.

When the number of cold gas inlets per circle increased from three to six, σ_T , σ_V , and Δt showed a decreasing trend. When the number reached the value of six, the mixing results no longer changed significantly; σ_V and Δt even increased. Under the constant total inlet flow rate, the increase in the number of cold gas inlets per circle increased the

collision of cold and hot gases, which reduced the flow rate per inlet. Thus, the number of cold gas inlets per circle should not be large. Therefore, the value of six was selected as an optimal value of the number of cold gas inlets per circle in this study.

Table 4 Mixing results for different numbers of cold gas inlets

numbers of cold gas inlets per circle	σ_T	σ_V	Δt (s)
3	35.8	1.5	7.3
4	26.1	1.4	5.8
5	24.5	1.1	4.7
6	22.1	0.86	4.5
7	21.7	0.94	4.8
8	21.9	0.83	5.1
9	22.3	1.2	4.7
10	21.5	1.3	5.9

3.2 Column Number of Cold Gas Inlets

As explained in Section 3.1, the mixing performance could be improved by appropriately increasing the number of cold gas inlets. In addition to increasing the number of cold gas inlets per circle, a similar effect could be achieved by increasing the column of cold gas inlets. In the test, the number of cold gas inlets per circle was set to six, and structures with a different number of columns of cold gas inlets were analyzed, as shown in Fig. 9.

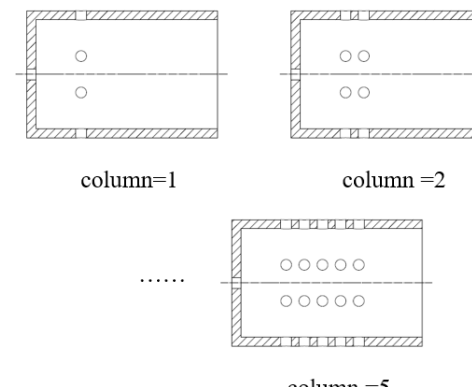


Fig. 9. Structures with a different number of columns of cold gas inlets.

The mixing performances of structures with a different number of columns are shown in Table 5.

Table 5 Mixing performances of structures with a different number of columns of cold gas inlets

Number of columns	σ_T	σ_V	Δt (s)
1	22.1	0.86	4.5
2	20.1	0.73	4.2
3	17.3	0.63	3.4
4	16.6	0.93	4.4
5	16.2	1.05	4.9

According to the results, using more columns of cold gas inlets increased the heat exchange area but reduced the flow rate of each hole. When the number of columns of cold gas inlets increased from one to three, σ_T showed an obvious decreasing trend; when the number of columns reached the value of three, the decreasing trend of σ_T reduced, while σ_V and Δt first decreased and then increased. When the number of columns was larger than three, the mixing results no longer changed significantly. Considering the structural complexity, three columns of cold gas inlets were regarded as the optimal choice.

3.3 Injection Angle

The injection angle of cold gas inlets can also affect the mixing performance. The effects of the axial injection angle α and tangential injection angle β were analyzed, keeping the other parameters fixed. The injection angle curve of the cold gas inlets is presented in Fig. 10, and the mixing results obtained for different axial injection angles are given in Table 6.

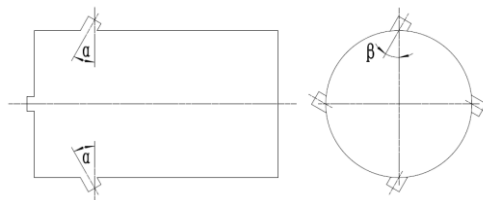


Fig. 10. Injection angle curve of cold gas inlets.

Table 6 Mixing results for different axial injection angles.

α (°)	σ_T	σ_V	Δt (s)
-45	39.7	1.03	9.6
-30	29.3	0.87	8.8
0	26.1	1.4	7.3
30	26.4	0.81	7.4
45	46.1	0.90	7.1

By keeping the other parameters unchanged, the mixing results were analyzed for different tangential injection angles, and the obtained results are shown in Table 7.

Table 7 Mixing results for different tangential injection angles

β (°)	σ_T	σ_V	Δt (s)
-45	26.4	1.64	8.8
-30	41.4	0.87	8.4
0	26.1	1.4	5.8
30	42.6	0.79	9.1
45	28.3	1.46	10.3

The results indicated that the effect of the injection angle was complex. The axial injection in the opposite direction to the hot gas was beneficial for the intensification of the interaction between different temperature gases. However, when the angle α was too large, the airflow radial velocity decreased, and the cold gas could not reach the chamber center, which resulted in inhomogeneity of the temperature field. The results demonstrated that Δt showed a downward trend with the increase in axial injection angle α ; σ_T increased with the absolute value of α . There was no significant change in σ_V as α varied. The mixing results show symmetry with the change in the tangential injection angle β . The mixing performance was better when the angle β was zero.

3.4 Orifice Plate Diversion

The orifice plate can affect the airflow distribution. As shown in Fig. 11, the hot gas passed through the orifice plate before mixing with the cold gas, so multiple streams of the hot gas increased the mixing area with the cold gas. Considering the symmetry, the number of holes on the orifice plate should be the same as the number of cold gas inlets per circle. The mixing results obtained with and without the orifice plate diversion are shown in Table 8. The orifice plate diversion reduced the mixing speed slightly but improved the uniformity of outlet airflow.

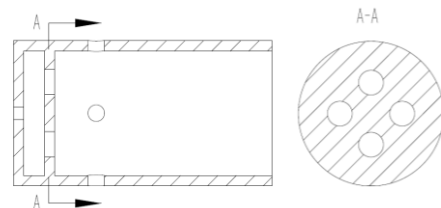


Fig. 11. A mixing chamber with an orifice plate.

Table 8 Mixing results with and without the orifice plate diversion

	σ_T	σ_V	Δt (s)
Without orifice plate diversion	26.1	1.4	5.8
With orifice plate diversion	15.3	0.87	7.3

4. GAS MIXING CHAMBER OPTIMIZATION

By using the CFD method, the effects of different structural parameters on the mixing result were analyzed, as presented above. To realize an accurate description of the mixing effect, a series of sampling points at the outlet section were selected. The temperature and velocity of the selected sampling points were monitored by calculating the standard

deviation σ_T and σ_V values. These two parameters were used to describe the uniformity of the mixed airflow. Smaller values of σ_T and σ_V indicated that the airflow at the outlet was more uniform. The mixing speed was measured by the time Δt necessary to reach a steady state.

To investigate the effects of the number and distribution of cold air inlets and the orifice plate on the mixing performance, this study used the control variates method to analyze the changing trend of the mixing result with different parameters. The results indicated that an appropriate increase in the number of cold gas inlets resulted in a more uniform airflow at the outlet but shortened the mixing time. In addition, increasing the heat exchange area of hot and cold gases improved the performance of the mixing chamber. This could also be achieved by adding an orifice plate to disperse the hot gas.

However, there were certain limitations in the analysis by the control variate method. Namely, the coupling effect between different parameters was not considered. In addition, as the considered parameters' values increased, more time and computer resources were needed to simulate each combination using the control variates method. The control variate method could not obtain the global optimal solution in the design space. Therefore, to obtain the optimal gas mixing chamber structure, a better parameters optimization method is required.

4.1 Initial Structure of Gas Mixing Chamber

According to the analysis in Section 3, six cold gas inlets per circle and three columns of inlets were used in the initial design of a gas mixing chamber. Considering the circumferential symmetry, the number of holes on the orifice plate was set to six. The simplified 3D model of the initial design of a gas mixing chamber is shown in Fig. 12.

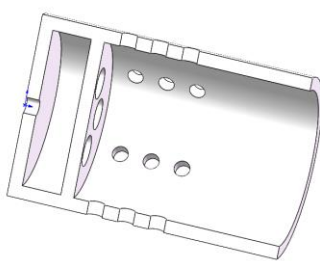


Fig. 12. Simplified 3D model of a mixing chamber.

The diameters of the cold and hot gas inlets were 6 mm. The design variables to be optimized are shown in Fig. 13.

The initial values of all parameters are shown in Table 9, where α_i and β_i ($i=1, 2, 3$) are the axial and

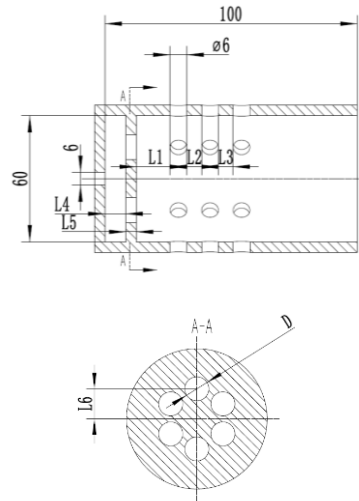


Fig. 13. Mixing chamber parameters.

Table 9 Initial values

Parameter (mm)	Value	Parameter (°)	Value
L_1	6	α_1	0
L_2	6	α_2	0
L_3	6	α_3	0
L_4	15	β_1	0
L_5	5	β_2	0
L_6	15	β_3	0
D	12		

tangential injection angles of the i th column cold gas inlet, respectively.

4.2 Optimization Method

The optimization problem of the gas mixing chamber can be described as follows:

$$\left\{ \begin{array}{l} \text{Find: } X = [L_1, L_2, L_3, L_4, L_5, L_6, D, \alpha_1, \alpha_2, \alpha_3, \beta_1, \beta_2, \beta_3]^T \\ \left\{ \begin{array}{l} \text{Minimize: } \sigma_T \\ \text{Minimize: } \sigma_V \\ \text{Minimize: } \Delta t \end{array} \right. \\ \text{S.T.: } X \in \Psi(X) \end{array} \right.$$

where $\Psi(X)$ is the design space of variables.

The value ranges of the parameters are shown in Table 10. The optimization problem is equivalent to finding a set of optimal values of design variables $X = [L_1, L_2, L_3, L_4, L_5, L_6, D, \alpha_1, \alpha_2, \alpha_3, \beta_1, \beta_2, \beta_3]^T$ in the design space that meet the design objectives.

The optimization of the gas mixing chamber design is a multi-objective optimization problem that involves several design variables. Currently, there are two common methods to handle multi-objective optimization problems, which are as follows:

Table 10 Design space

Variable	Initial value	Lower boundary	Upper boundary
L_1 (mm)	6	3	15
L_2 (mm)	6	3	15
L_3 (mm)	6	3	15
L_4 (mm)	15	5	20
L_5 (mm)	5	3	10
L_6 (mm)	15	10	25
D (mm)	12	6	15
α_1 (°)	0	-60	60
α_1 (°)	0	-60	60
α_1 (°)	0	-60	60
β_1 (°)	0	-60	60
β_2 (°)	0	-60	60
β_3 (°)	0	-60	60

- 1) Normalization method: This method converts a multi-objective optimization problem into a single-objective optimization problem and calculates an optimal solution under a single combination of weights;
- 2) Multi-objective optimization: This method uses a multi-objective optimization algorithm to calculate an optimal solution with all regroups and obtain the set of Pareto solutions.

The disadvantages of the normalization method are obvious. Namely, the weighting factor is subjectively determined, and a sub-objective's superiority progress is not actionable. Therefore, in this study, the second-generation non-dominated sorting GA (NSGA-II) method is used. The NSGA-II method represents an improved version of the first generation of the non-dominated sorting GA (NSGA). Compared to the NSGA, the NSGA-II applies a faster non-dominated sorting algorithm, which reduces the computational complexity significantly. Moreover, the NSGA-II searches for the global optimum in the entire design space.

4.3 Sensitivity Analysis

To make the optimization process more efficient, a sensitivity analysis was performed to investigate the effect of the input variables on the design objectives ([Etesami *et al.* 2021](#)).

The Spearman correlation method was used to measure a monotonic relationship between two variables. The range of the Spearman coefficient (ρ) was from -1 to +1. A smaller absolute value of the Spearman correlation coefficient indicated that the input had less influence on the output value. When the average Spearman correlation value was less than 0.1, it was assumed that there was no correlation between the variables. The Spearman correlation value was obtained by Eq. (4), where m is the number of samples, and d represents the equivalence difference between two series of data.

$$\rho = 1 - \frac{6 \sum d_i^2}{m(m^2 - 1)} \quad (4)$$

The Design of Experiments (DOE) can be used to analyze the relationships and trends between input and output parameters ([Wang *et al.* 2017](#)).

Table 11 Correlation coefficient result

Variable	σ_T	σ_V	Average correlation $\bar{\rho}$
L_1	0.20	0.14	0.17
L_2	0.41	0.24	0.325
L_3	0.12	0.44	0.28
L_4	0.12	0.06	0.09
L_5	0.42	0.25	0.335
L_6	-0.37	0.42	0.395
D	0.39	-0.08	0.235
α_1	-0.26	-0.22	0.24
α_1	0.07	0.39	0.23
β_1	-0.05	0.36	0.205
β_2	-0.04	0.08	0.06
β_3	-0.27	-0.43	0.35

In this study, the Optimal Latin hypercube design (OLHD) was selected considering that all test points were distributed as evenly as possible in the design space. The OLHD has a better performance in space-filling and balance compared to the Latin hypercube design (LHD) ([Zhang *et al.* 2021](#); [Soheil and Daryan 2021](#)).

The correlation coefficient table obtained by the DOE is shown in Table 5. The input geometry variables β_2 and L_4 were omitted since their average correlation values were less than 0.1.

4.4 NSGA-II Optimization

The NSGA-II multi-objective optimization algorithm and self-defined components were integrated into the ISIGHT platform to perform the parameter optimization of the mixing chamber ([Silva *et al.* 2021](#)). The simcode component in ISIGHT can read or write text files and execute relevant system commands. In the optimization process, the program could use other software and perform related operations by the simcode component.

The optimization process is shown in Fig. 14.

The specific steps of the NSGA-II method were as follows:

Step 1: Determine optimization parameters by sensitivity analysis;

Step 2: Initialize the population; generate an initial set of parameters in the design space to be used as input parameters of the Catia module;

Step 3: Complete the geometric modeling using the input parameters and the Catia module. Then, call

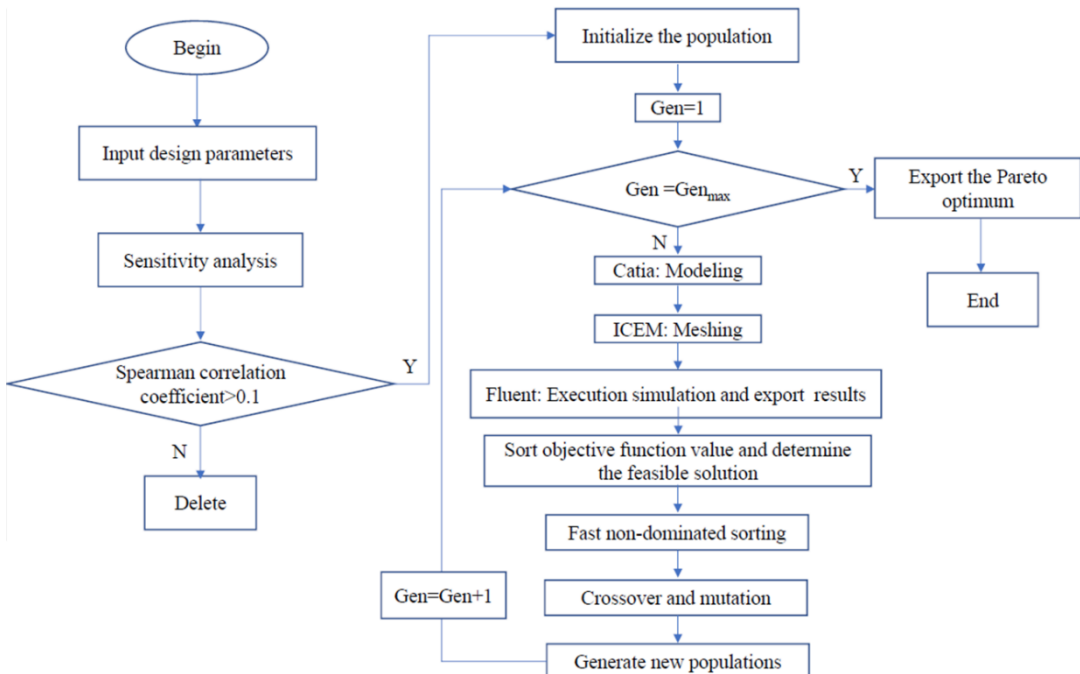


Fig. 14. Optimization process.

ICEM for meshing and generate a mesh file. Complete numerical simulation and export target parameters using the Fluent module to obtain the objective function results;

Step 4: Assess the fitness function of the initial population and perform a fast non-dominated sorting method. Obtain new populations by cross-variation;

Step 5: Determine if the maximum number of iterations has been reached. If not, repeat Steps 2–4; otherwise, export the Pareto optimal solution.

4.5 RESULTS

The GA parameters selected were as follows: mutation rate was 0.02, and crossover rate was 0.6; 30% of the best optimal individuals were retained into the next generation. The GA selected a population of 16 candidates and a total of 10 generations. Selecting an optimal value of the eighth generation, the σ_T of the optimal result was 14.7, the σ_v of the optimal result was 0.36, and the mixing time Δt was 3.2 s. The optimized structural parameters of the gas mixing chamber were: $x = [L_1, L_2, L_3, L_4, L_5, L_6, D, \alpha_1, \alpha_2, \alpha_3, \beta_1, \beta_2, \beta_3]^T = [18.6, 6.4, 8.3, 15, 4.3, 16, 14, 13, 16, -38, 10, 0, -23]$. The structure of the optimized mixing chamber is shown in Fig. 15.

The NSGA-II achieved a satisfying result as shown in table 6. This optimization method decreased the σ_T and σ_v values, which resulted in a more uniform distribution of temperature, and the mixing time decreased from 4.4 s to 2.3 s.

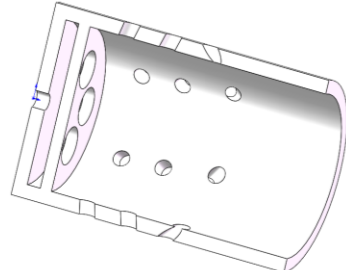


Fig. 15. Optimized mixing chamber structure.

Table 12 Mixing performance of the optimized gas mixing chamber

Performance	Base	Optimized
σ_T	25.2	14.7
σ_v	1.3	0.36
$\Delta t/s$	4.4	2.3

Then, the optimization was performed again based on the CFD analysis, as shown in Fig. 16.

Compared to the initial gas mixing chamber, the injection angle and location of cold gas inlets in the optimized gas mixing chamber were changed; namely, the temperature and velocity curves of the optimization result were more evenly distributed.

5. EXPERIMENTAL RESULTS

Based on the optimized mixing chamber structure, a mixing chamber experimental platform was constructed, as shown in Fig. 17. Since the airflow

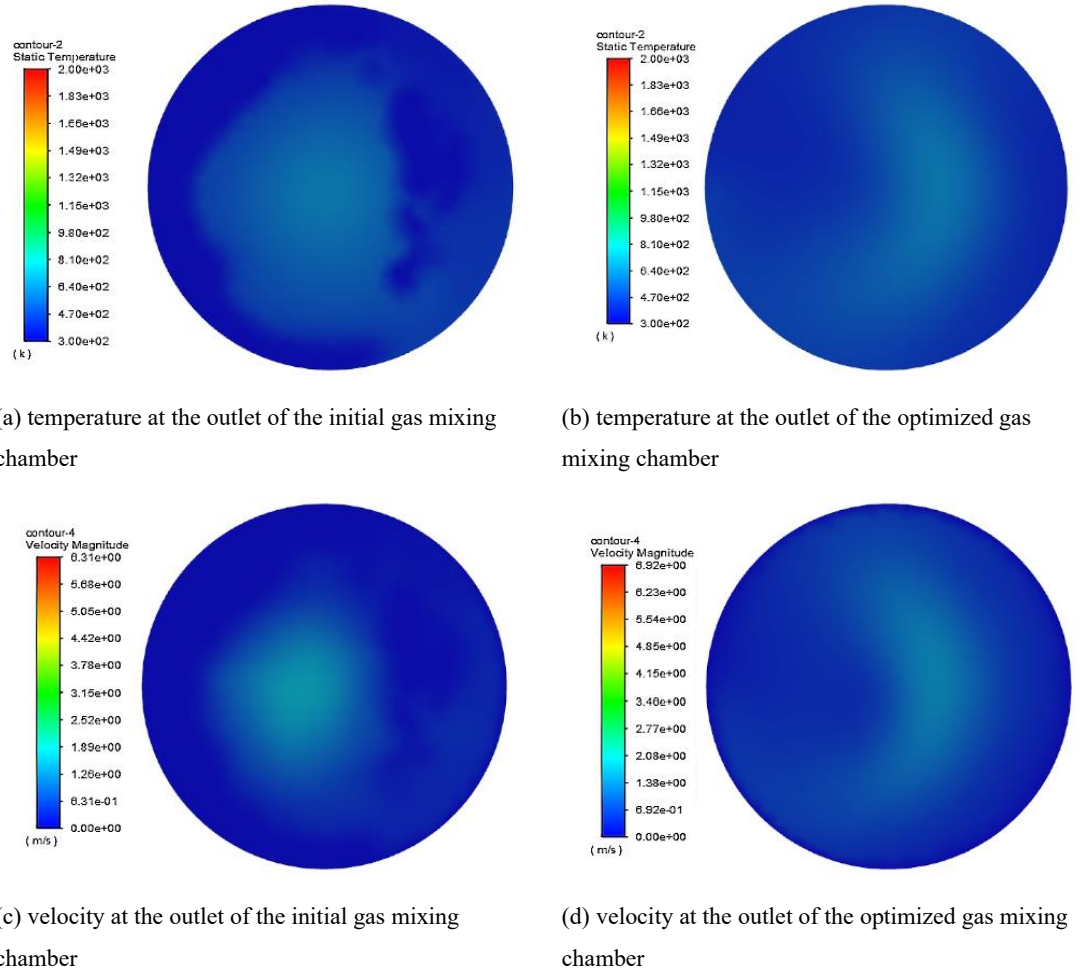


Fig. 16. Comparison of the mixing results at the outlet.

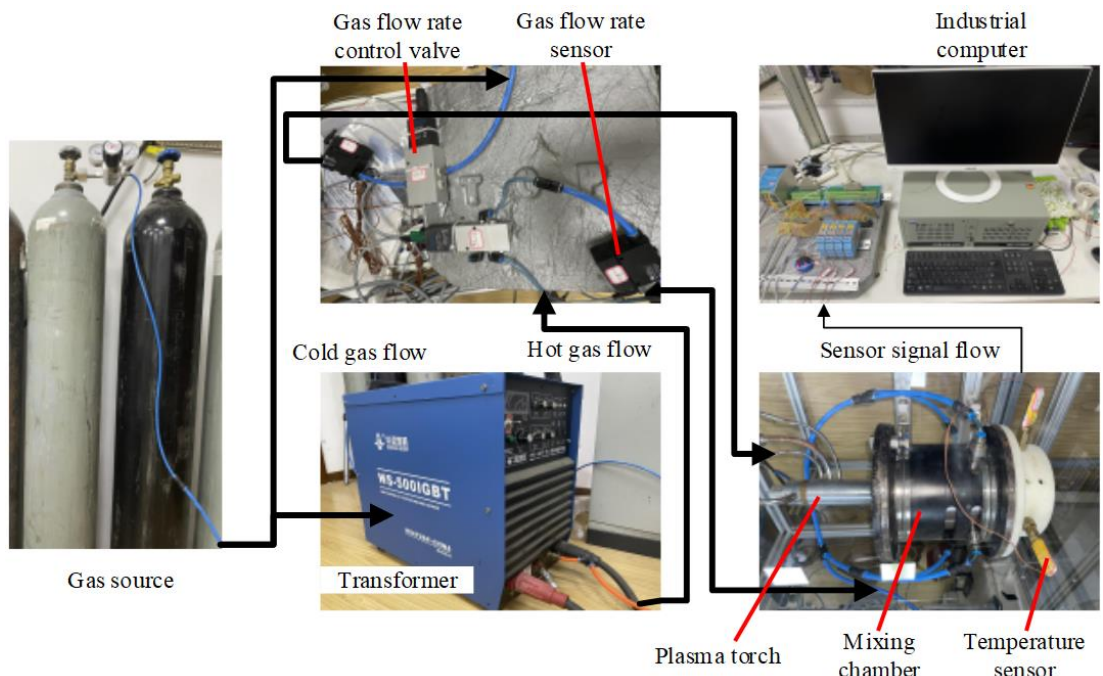


Fig. 17. Experimental platform of the mixing chamber.

velocity at the outlet in the experiment could not be measured easily, the correctness of the simulation model was evaluated using the temperature value and its standard deviation. The temperature at the outlet was measured, as described in the following. Considering the installation of the temperature sensor and the adjustment of the measurement point, 16 points were selected as measurement points at the outlet plane, as shown in Fig. 18. Four temperature sensors were used to measure the temperature values of the selected points. To compare the simulation and experimental results, 16 points at the same position on the outlet plane as those in the simulation model were selected as measurement points, and the same cold and hot air flows and temperature values were set in the simulation and experiment.

By using the same simulation model as described above and the same actual experiment conditions, the temperature and flow rate of the hot gas flow were adjusted. The hot air temperature was 4,350 K, the flow rate was 5 L/min, and the cold air flow was 20 L/min. The average outlet temperature curve is shown in Fig. 19(a). The mixing time Δt in the experiment was 6.15 s, while that in the simulation was 3.75 s. Thus, there was a certain difference in the mixing time between the experiment and the

simulation. This was because the heat transfer process between the sensor and the gas flow to be measured was not considered in the simulation.

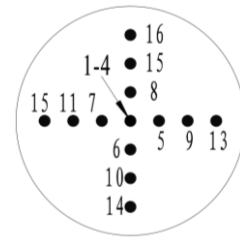


Fig. 18. Distribution of the measurement points.

After the mixing process finished, the average temperature of the outlet in the experiment was 812.50 K, while that in the simulation was 805.02 K. The temperatures of the 16 selected monitoring points in the simulation and test outlets are shown in Fig. 19(b). The standard deviations of the outlet temperatures obtained by the experiment and simulation were 39.11 and 12.62, respectively. Thus, the experimental and simulation results were in good agreement

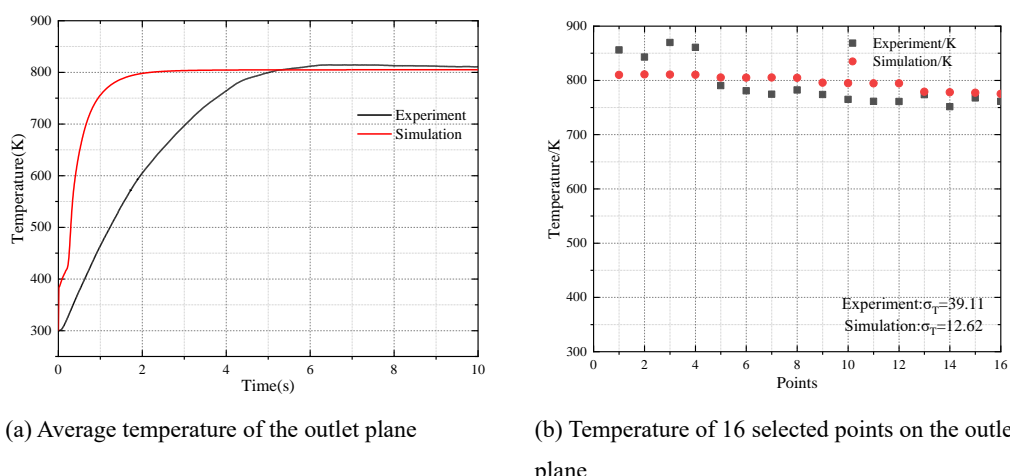


Fig. 19. Temperature of the outlet plane 0at the cold gas flow rate of 20 L/min.

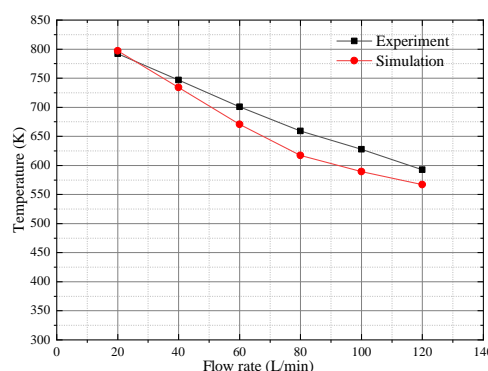


Fig. 20. Temperature at the outlet plane at different cold gas flow rates.

To illustrate the problem further, five groups of control experiments were performed at the cold air flow rates of 40 L/min, 60 L/min, 80 L/min, 100 L/min, and 120 L/min. The average temperature at the outlet under different cold air flow conditions is shown in Fig. 20, where it can be seen that the simulation and experimental results were relatively consistent regardless of the cold air flow change.

The temperature distributions of the 16 monitoring points at the outlet obtained in the simulation and experiment were determined, and their standard deviations were calculated. As shown in Figs. 21(a)–21(e), the outlet temperature distribution and standard deviation showed similar trends in the experiment and simulation at different flow rates.

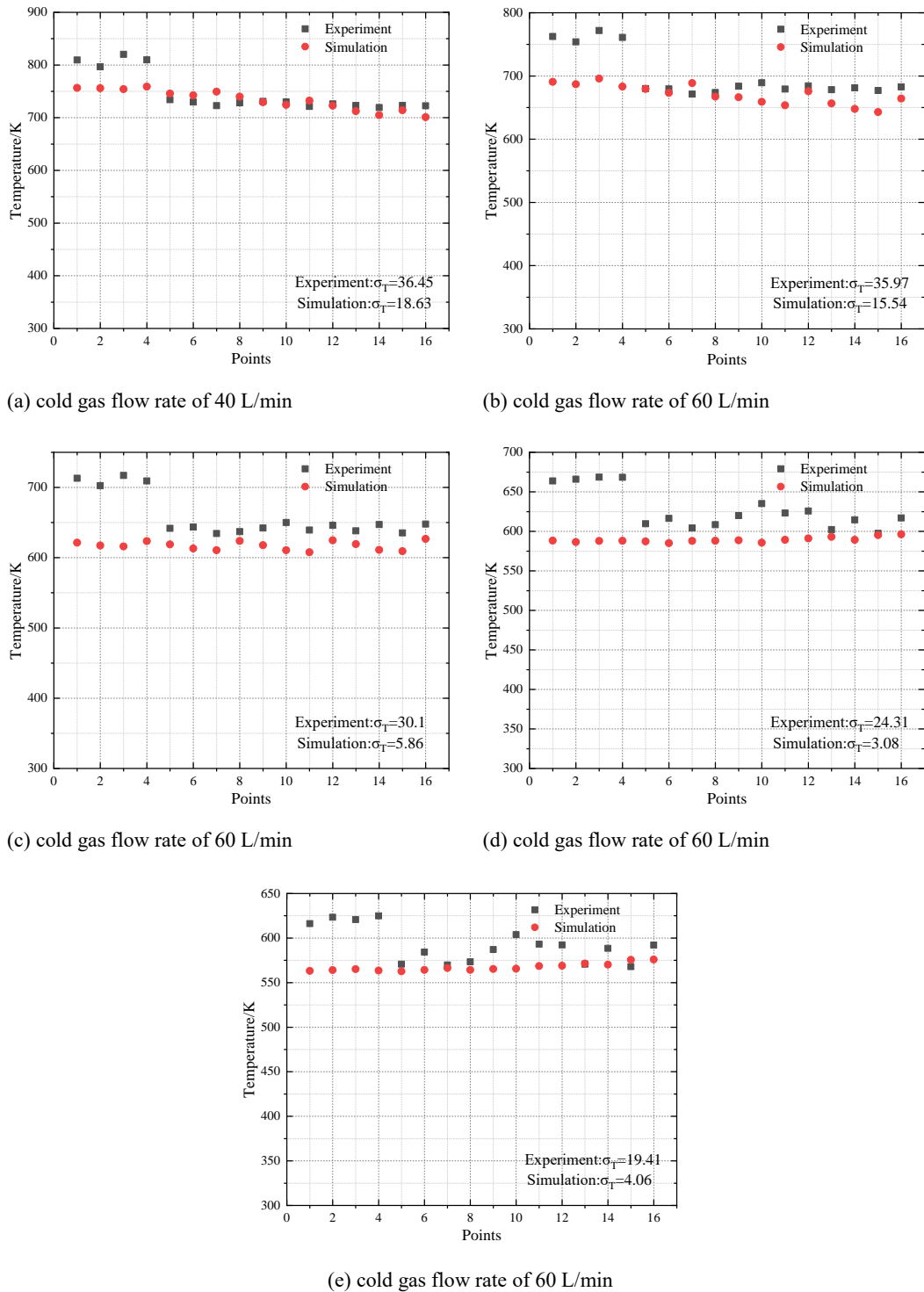


Fig. 21. Temperature at the outlet plane at different cold gas flow rates.

The consistency in the simulation and experimental data has proven the correctness of the proposed simulation method. Based on the chamber characteristics simulation and optimization processes presented above, it can be concluded that the optimization results based on the proposed simulation method are locally optimal. Therefore, the structure optimization of the cold and hot airflow mixing chamber can improve the performance of the mixing chamber, thus improving the efficiency of the heat exchange between the cold and hot airflow mixing process.

6. CONCLUSIONS

To improve the heat exchange efficiency of hot and cold gas flows, which allows a specific uniform temperature field can be obtained faster, an optimization method based on the GA is used to optimize the chamber structure. The experimental and simulation results are consistent, which verifies that the CFD simulation method used in this study is correct. In addition, it is demonstrated that a more efficient mixing of the cold and hot gas flows can be achieved when the chamber structure is optimized.

The main conclusions are as follows:

- The structural parameters of the mixing chamber, such as the number of cold gas inlets, affect the mixing efficiency of the chamber;
- Three columns of cold gas inlets and six gas inlets per column are the optimal parameters of the mixing chamber in terms of improving the mixing performance;
- The simulation results show that the gas mixing chamber optimized by the NSGA-II can significantly reduce the temperature mixing degree σ_T from 25.2 to 14.7, the velocity mixing degree σ_V from 1.3 to 0.36, and the mixing time from 4.4 s to 2.3 s;
- The experiment results of the optimized structure show that the real mixing time is 6.15 s, σ_T is 39.11, and the cold gas flow rate is 20 L/min.

In summary, the proposed optimized mixing structure of the cold and hot air flow chamber can realize rapid and uniform mixing of the cold and hot gas flows. The experiment results show that after the chamber structure optimization, the mixing efficiency of the cold and hot gas flows is improved, as well as the mixing performance of the chamber. The method proposed in this paper can provide a reference for the optimization of similar structural parameters and the implementation of temperature simulation equipment.

ACKNOWLEDGMENT

The research presented in this paper was supported by the National Natural Science Foundation of China

under Grant No. 51975223. We thank LetPub (www letpub.com) for its linguistic assistance during the preparation of this manuscript.

CONFLICT OF INTEREST STATEMENT

On behalf of all authors, the corresponding author states that there is no conflict of interest.

REFERENCES

- Asif, M., R. Chaturvedi and A. Dhiman (2021). Heat transfer enhancement from inline and staggered arrays of cylinders in a heat exchanger using alumina–water nanofluid. *Journal of Thermal Science and Engineering Applications* 13(4), 041025.
- Badenhorst, H. (2020). Optimising graphite composites and plate heat exchangers for latent thermal energy storage using measurements and simulation. *Journal of Energy Storage* 29, 101347.
- Etesami, G., M. E. Felezi and N. Nariman-Zadeh (2021). Optimal transmission angle and dynamic balancing of slider-crank mechanism with joint clearance using Pareto Bi-objective Genetic Algorithm. *Journal of the Brazilian Society of Mechanical Sciences and Engineering* 43(4), 1-18.
- Filip, R. and T. Melichar (2021). Numerical Analysis of Heat Transfer on the Shell Side of a Helically Coiled Tube Heat Exchanger for Helium Applications. *Journal of Nuclear Engineering and Radiation Science* 7(2), 021403.
- Habibi, F. I., F. Hartono and H. Prayogo (2019). Optimization of an Annular Combustion Chamber for Micro Turbo Jet System. In *IOP Conference Series: Materials Science and Engineering*, Bandung City, Indonesia.
- Karana, D. R. and R. R. Sahoo (2021). Heat transfer and pressure drop investigations of the compact exhaust heat exchanger with twisted tape inserts for automotive waste heat utilization. *Journal of Thermal Science and Engineering Applications* 13(4), 041003.
- Mishra, M. and P. K. Das (2009). Thermoeconomic design-optimisation of crossflow plate-fin heat exchanger using Genetic Algorithm. *International Journal of Exergy* 6(6), 837-852.
- Mishra, M., P. K. Das and S. Sarangi (2004). Optimum design of crossflow plate-fin heat exchangers through genetic algorithm. *International Journal of Heat Exchangers* 5 (2), 379-402.
- Mishra, M., P. K. Das and S. Sarangi (2009). Second law based optimisation of crossflow plate-fin heat exchanger design using genetic algorithm.

- Applied Thermal Engineering 29(14-15), 2983-2989.
- Mizeraczyk, J., Z. Zakrzewski, M. Jasinski and M. Lubanski (2000). Decomposition of high-concentration NO in atmospheric pressure flowing Ar or N₂ using coaxial-line-based microwave torch plasma. In *Conference Record of the 2000 IEEE Industry Applications Conference. In Thirty-Fifth IAS Annual Meeting and World Conference on Industrial Applications of Electrical Energy*, Rome, Italy.
- Soheil P., and A. S. Daryan (2021). Critical Temperature Evaluation of Moment Frames by Means of Plastic Analysis Theory and Genetic Algorithm. *Iranian Journal of Science and Technology, Transactions of Civil Engineering* 46(2), 843-856.
- Riley, Z. B., R. A. Perez and G. W. Bartram (2019). Aerothermoelastic experimental design for the AEDC/VKF tunnel C: Challenges associated with measuring the response of flexible panels in high-temperature, high-speed wind tunnels. *Journal of Sound and Vibration* 441 (2), 96-105.
- Silva, R. C. C., J. M. P. de Menezes Júnior and J. M. de Araújo Júnior (2021). Optimization of narx neural models using particle swarm optimization and genetic algorithms applied to identification of photovoltaic systems. *Journal of Solar Energy Engineering* 143(5), 051001.
- Tang, S. Z., M. J. Li, F. L. Wang and Z. B. Liu (2019a). Fouling and thermal-hydraulic characteristics of aligned elliptical tube and honeycomb circular tube in flue gas heat exchangers. *Fuel* 251, 316-327.
- Tang, T., L. Gao, B. Li, L. Liao, Y. Xi and G. Yang (2019b). Cavitation optimization of a throttle orifice plate based on three-dimensional genetic algorithm and topology optimization. *Structural and Multidisciplinary Optimization* 60(3), 1227-1244.
- Vázquez, F. V., P. Simell, J. Pennanen and J. Lehtonen (2016). Reactor design and catalysts testing for hydrogen production by methanol steam reforming for fuel cells applications. *International Journal of Hydrogen Energy* 41(2), 924-935.
- Wang, W., H. Zhang, Z. Zhao, Q. Zheng and B. Bai (2017). Mixing of hollow-cone water spray in a confined high-temperature gas crossflow. *Computers & Fluids* 154, 216-223.
- Xie, C. and D. Wang (2020). Multi-objective cross-sectional shape and size optimization of S-rail using hybrid multi-criteria decision-making method[J]. *Structural and Multidisciplinary Optimization* 62(6), 3477-3492.
- Yan, Y. Y., H. C. Lio and T. F. Lin (1999). Condensation heat transfer and pressure drop of refrigerant R-134a in a plate heat exchanger. *International Journal of Heat and Mass Transfer* 42(6), 993-1006.
- Yee, T. F., I. E. Grossmann and Z. Kravanja (1990). Simultaneous optimization models for heat integration—III. Process and heat exchanger network optimization. *Computers & Chemical Engineering* 14(11), 1185-1200.
- Zhang, Z., J. Ma and X. Cui (2021). Genetic algorithm with three-dimensional population dominance strategy for university course timetabling problem. *International Journal of Grid and High Performance Computing* 13(2), 56-69.
- Zhao, K., L. I. Feng, L. U. Fuguo, Z. Tao and Y. Hongyu (2018). Probe design for measuring total temperature of combustor outlet based on water cooling. *Journal of Aerospace Power* 33(09), 2084-2092.
- Zhao, T., H. Tian, L. Shi, T. Chen, X. Ma, M. A. R. Atik and G. Shu (2020). Numerical analysis of flow characteristics and heat transfer of high-temperature exhaust gas through porous fins. *Applied Thermal Engineering* 165, 114612.
- Zhu, M. H., W. A. Xi, P. E. Xitong, S. Zhang, D. A. Zhihong, G. U. Nannan, Y. A. Shubo, M. I. Keqiang, C. H. Huairong and L. I. Jiashuai (2021). Modified robust optimal adaptive control for flight environment simulation system with heat transfer uncertainty. *Chinese Journal of Aeronautics* 34(2), 420-431.
- Zou, X. F., Guo, D. W. and Pan, K (2018). Combined strength test technology for hypersonic vehicle structures under integrated load (in Chinese). *Acta Aeronautica et Astronautica Sinica* 39(12), 222326.